

Article

# Metal content of relativistically jetted and radio-quiet quasars in the main sequence context

Paola Marziani<sup>1</sup>, Swayamtrupta Panda<sup>2</sup> Alice Deconto Machado<sup>3</sup>, Ascension Del Olmo<sup>3</sup>

<sup>1</sup> National Institute for Astrophysics (INAF), Astronomical Observatory of Padova, vicolo dell'Osservatorio 5, IT-35122 Padova, Italy

<sup>2</sup> Laboratório Nacional de Astrofísica, R. dos Estados Unidos, 154 - Nações, Itajubá - MG, 37504-364, Brazil

<sup>3</sup> Instituto de Astrofísica de Andalucía, IAA-CSIC, Glorieta de la Astronomía s/n, E-18008 Granada, Spain, chony@iaa.es (A.d.O.)

\* Correspondence: paola.marziani@inaf.it; Tel.: +39-0498293415

Version March 24, 2023 submitted to *Galaxies*

**Abstract:** Optical and UV properties of radio-quiet (RQ) and radio-loud (RL, relativistically "jetted") active galactic nuclei (AGN) are known to differ markedly; however, it is still unclear what is due to a sample selection and what is associated with intrinsic differences in the inner workings of their emitting regions. Chemical composition is an important parameter related to the trends of the quasar main sequence. Recent works suggest that in addition to physical properties such as density, column density, and ionization level, strong FeII emitters require very high metal content. Little is known, however, about the chemical composition of jetted radio-loud sources. In this short note, we present a pilot analysis of the chemical composition of low-*z* radio-loud and radio-quiet quasars. Optical and UV spectra from ground and space were combined to allow for precise measurements of metallicity-sensitive diagnostic ratios. The comparison between radio-quiet and radio-loud was carried out for sources in the same domain of the Eigenvector 1 / main sequence parameter space. Arrays of dedicated photoionization simulations with the input of appropriate spectral energy distributions indicate that metallicity is sub-solar for RL AGN, and slightly sub-solar or around solar for RQ AGN. The metal content of the broad line emitting region likely reflects a similar enrichment story for both classes of AGN not involving recent circum-nuclear or nuclear starbursts.

**Keywords:** active galactic nuclei; optical spectroscopy; ionized gas; broad line region; interstellar medium; chemical composition; individual quasar: PKS0226-038; photoionization; radiative transfer

## 1. Introduction

Type-1 active galactic nuclei (AGN) are characterized by the presence of broad and narrow optical and UV lines (for an introduction, see e.g., [1–3]). AGN spectra show a mind-boggling variety of broad emission line profiles not only among different objects but also among different lines in the spectrum of the same object. For stars, the identification of optical spectral types and luminosity classes allows for the knowledge of the most relevant physical parameters, including the star's evolutionary status [4]. This feat is not as yet possible for AGN. Although, progress in the empirical classification has yielded a coarse contextualization of the main accretion properties, such as black hole mass, Eddington ratio, outflow prominence, spectral energy distributions, emitting region size, the metal content of the line emitting gas, etc. [e.g., 5–11]. The main set of correlations was derived from a principal component analysis (PCA) on a sample of several tens of quasars [12]. The importance of the Eigenvector 1 derived from the PCA has revealed itself over the years [13], leading to the definition of what has become known as the main sequence of quasars [14,15]. The optical plane of this main sequence is identified by the line width of the H $\beta$  Balmer line  $H\beta$  (FWHM  $H\beta$ ) and the prominence of a singly-ionized emission,

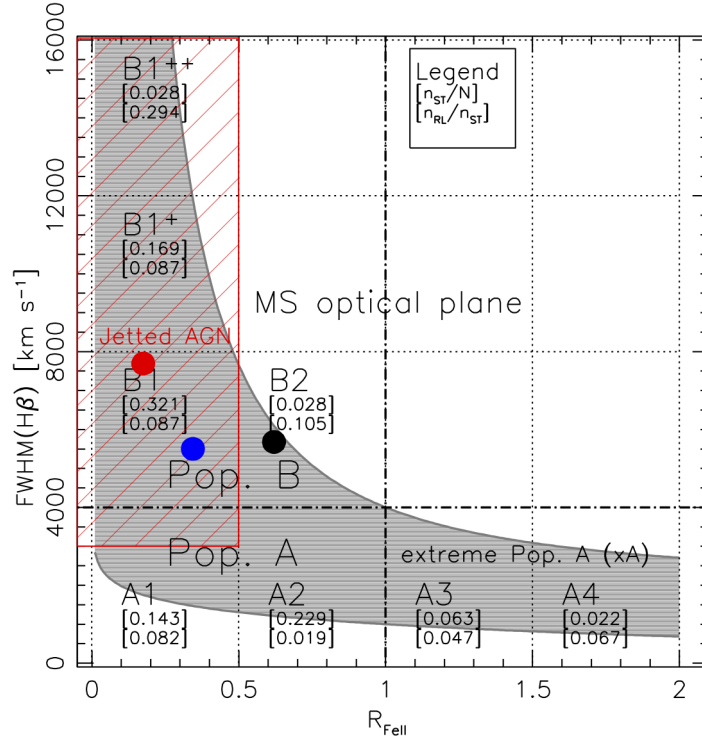


**Figure 1.** Sketch of the optical plane of the MS, FWHM  $H\beta$  vs.  $R_{FeII}$ . Numbers in square brackets provide, from top to bottom, the complete sample fractional occupation, the fraction of jettted (core-dominated + Fanaroff-Riley II) sources in each spectral bin. The shaded area identifies the region along the sequence with a high prevalence of jettted sources (c.f. Ref. [18]). The original sample is described in Ref. [19]. Points mark the location of the composite spectra (red: RL; blue: RQ) and of PKS 0226-038 (black).

defined as the flux ratio between the FeII blends centered at  $\lambda 4570$  and  $H\beta$  itself (hereafter  $R_{FeII}$ ). The distribution of type 1, unobscured AGN takes the form of an elbow-shaped sequence in the optical plane (see e.g., Figure 1). The ranges of  $R_{FeII}$  and FWHM  $H\beta$  define spectral types [15,16], and different classes may show different occupations in the plane (Figure 1). A case in point is provided by RQ and RL [17]: most powerful, relativistically jettted sources cluster in Population B - with moderate FeII emission and relatively broad  $H\beta$  line profiles ( $4000 \text{ km s}^{-1} \lesssim \text{FWHM}(H\beta) \lesssim 8000 \text{ km s}^{-1}$ ). The broader spectral type shows higher fractions of RL; however, these spectral bins have a low prevalence, and a sizeable fraction of all type 1 AGN falls only in bin B1. This spectral type is, therefore, well suited for an inter-comparison between RQ and RL properties. In the following, we will build composite spectra for jettted and non-jettted sources of spectral type B1 (§ 2). The analysis takes advantage of the main sequence (MS) correlations concerning line profiles in the spectral type B1 (§ 3). It's focused on the measurements of intensity ratios intended to be diagnostics of the metal content of the line emitting gas. Intensity ratios are interpreted using arrays of photoionization simulations covering a broad range in metallicity. Results (§ 4) suggest slightly sub-solar or solar metallicity and provide evidence of significant diversity in terms of chemical enrichment and evolutionary status along the main sequence (§ 5).

## 2. Composite spectra for spectral type B1 quasars

To obtain spectral data of good quality covering the full spectral ranges from  $1000 \text{ \AA}$  to  $\approx 6000 \text{ \AA}$  (i.e., from  $Ly\alpha$  to  $H\beta$  included) for the same object is still a non-trivial feat for low- $z$  quasars, as the UV coverage demands space-based observations. Here, we consider one sample of 20 RL and one sample of 16 RQ sources, all belonging to spectral type B1, in the redshift range  $\approx 0.002 - 0.5$  and  $\approx 0.25 - 0.65$ ,

for RQ and RL respectively. The absolute magnitudes derived from the quick look magnitudes in the *NASA Extragalactic Database* (NED), and the range is between  $-21$  and  $-27$  (RQ), and between  $-23.5$  and  $-26.5$  (RL), which correspond to bolometric luminosities in the range  $\log L \sim 45 - 47$  [ $\text{erg s}^{-1}$ ]. The UV data are HST/FOS observations analyzed in Ref. [20], and the optical spectra were obtained from Ref. [19]. The spectral similarity ensures consistency of black hole mass and Eddington ratio. We built median and average composites for the RQ and RL classes that look consistent. As the median combination is not improving the S/N, the fitting analysis was performed only on the averages. The average S/N is high with  $S/N \approx 90$  for the RQ composites, and  $\approx 130$  and  $\approx 55$  for the visual and UV ranges in the RL composite, respectively. The composite spectra are shown in Figure 2.

### 3. Analysis

#### 3.1. Line profiles

Pop. B  $H\beta$  profiles show a redward asymmetry modeled with a broader redshifted (FWHM  $\sim 10000 \text{ km s}^{-1}$ , shift at line base  $\sim 1000 - 2000 \text{ km s}^{-1}$ ) and a narrower Gaussian [16,21]. The very broad Gaussian component is meant to represent the innermost part of the broad line region (BLR), providing a simple representation of the radial stratification of the BLR in Pop. B suggested by reverberation mapping [22]. This component (hereafter the very broad component, VBC) has been associated with a physical region of high-ionization virialized gas and closest to the continuum source - the very broad line region, VBLR [23–26]. While the physical properties of the VBLR line emitting gas are not well known, a decomposition of the full  $H\beta$  profile into a symmetric, unshifted  $H\beta$  component ( $H\beta_{\text{BC}}$ ) and a  $H\beta_{\text{VBC}}$  provide an excellent fit to most  $H\beta$  Pop. B profiles [16,27].

The multicomponent fits were performed using the SPECFIT routine from IRAF [28]. This routine allows for the simultaneous minimum- $\chi^2$  fit of the continuum approximated by a power law and the spectral line components yielding FWHM, peak wavelength, and intensity for all line components. In the optical range, we fit the  $H\beta$  profile and the [OIII] $\lambda\lambda 4959, 5007$  emission lines, and the FeII multiplets for the composite objects.

#### 3.2. Diagnostics of Metallicity and photo-ionization modeling

Diagnostics from the rest-frame UV spectrum take advantage of the observations of strong resonance lines that are collisionally excited [29,30] and at least constrain density  $n_{\text{H}}$ , ionization parameter  $U$ , and chemical abundance  $Z$ . For instance, C IV $\lambda 1549$ /Ly $\alpha$ , C IV $\lambda 1549$ /(Si IV + O IV) $\lambda 1400$ , C IV $\lambda 1549$ /He II $\lambda 1640$ , N V $\lambda 1240$ /He II $\lambda 1640$  are sensitive to metallicity; and Al III $\lambda 1860$ /Si III $\lambda 1892$ , Si III $\lambda 1892$ /C III $\lambda 1909$  are sensitive to density, since inter-combination lines have a well defined critical density [29,31]. Ratios of lines involving different ionic stages of the same element are obviously sensitive to the ionization parameter. The lines emitted from ionic species of Silicon and Aluminium deserve special attention - they are two elements greatly enhanced in Supernova ejecta [32]. This approach has yielded tight constraints, especially for sources radiating at high Eddington ratio [29,33,34], where physical properties are consequently well-constrained because they converge toward an extreme.

The photo-ionization code *Cloudy* [35] models the ionization, chemical, and thermal state of gas exposed to a radiation field and predicts its emission spectra and physical parameters. *Cloudy* simulations require inputs in terms of  $n_{\text{H}}$ ,  $U$ ,  $Z$ , quasar spectral energy distribution (SED), and column density  $N_{\text{c}}$ . The ionization parameter  $U = Q(H)/4\pi r_{\text{BLR}}^2 c n_{\text{H}}$ , where  $Q(H) = \int_{\nu_0}^{\infty} L_{\nu}/h\nu$  is the number of ionizing photons, provides the ratio between photon and hydrogen number density and is dependent on the spectral energy distribution of the ionizing continuum. The simulations were carried out assuming the RL and RQ SEDs from Laor et al. [36] representative of the SED of B1 objects (work in preparation). The geometry was assumed open, plane-parallel, meaning that a slab of emitting gas

is exposed to a radiation field only on one side. Arrays of *Cloudy* photo-ionization models<sup>1</sup> for a given metallicity  $Z$  and column density  $N_c$ , constant density  $n$  and ionization parameter  $U$  were evaluated at steps of 0.25 dex covering the ranges  $7 \leq \log n_{\text{H}} \leq 13$  [ $\text{cm}^{-3}$ ],  $-3 \leq \log U \leq 1$ . The single-value metallicity arrays were computed for  $\log Z$  at  $-3.0, -2.7, -2.3, -2.0, -1.7, -1.3, -1.0, -0.7, -0.3, 0, 0.3, 0.7, 1.0$ , and  $1.3$  in solar units, i.e. from  $0.001 Z_{\odot}$  to  $20 Z_{\odot}$ . No dust and no microturbulence broadening were included in the calculations. The  $Z$  calculations are based on a single zone assumption for the BLR. The lowest values of the density may bias the solutions toward cases where significant [OIII] $\lambda\lambda 4959, 5007$  is expected; all cases with [OIII] $\lambda 5007/H\beta > 0.1$  were excluded, as no broad [OIII] $\lambda\lambda 4959, 5007$  is observed. A more refined analysis in the framework of the locally optimized emitting cloud model [37–39] is deferred to an eventual work.

## 4. Results

### 4.1. Composite spectra

The composite average spectra are shown in Figure 2. The spectral similarity between the two classes already evident in Figure 2 is confirmed by the profile comparison of Fig. 3. Both spectra are FeII weak; show weak NV; AlIII is weak while the CIII] line is by far the most prominent in the 1900 Å blend encompassing SiIII] and CIII] along with AlIII. All lines can be successfully decomposed into a BC and a VBC. Apparently, there is no VBC in the AlIII and SiIII] lines and in FeII. No prominent BC is observed in the HeII optical and UV lines, at variance with  $H\beta$ ,  $Ly\alpha$ , CIV, and the other lines. The absence of a prominent BC in Helium lines is typical [40], albeit the implications for the BLR structure are not obvious even on a qualitative basis. Table 1 reports the line fluxes normalized to  $H\beta$ . In view of the heuristic decomposition approach, fluxes are reported for the BC, VBC, and sum of the two components, i.e., for the full broad profile (total flux). Each value in this table has been normalized by the corresponding component of  $H\beta$ . Error analysis has been performed empirically or on the basis of previous analyses ( $H\beta$  and FeII: Refs. [19,41]; CIV: [42]; blend at 1900 Å: Refs. [34,41]; NV: Ref. [33]). The undetected HeII BC was considered in the models as  $\text{HeII}/H\beta \lesssim 0.1$ . A more refined treatment of uncertainties is deferred to future work.

Spectral differences between the two classes are not striking on a qualitative basis. We note a stronger redward asymmetry in RL sources. This is, however, a result known for a long time [43,44]. The optical FeII emission is twice as strong in RQ than in RL; this is also consistent with previous results [45]. The intensity ratios most commonly used in  $Z$  estimates are marginally higher for RQ than for RL.  $\text{SiIV}+\text{OIV}] \lambda 1402/\text{CIV}$ ,  $\approx 0.24$  vs  $0.15$  for RQ and RL, respectively. Similarly,  $\text{AlIII}/\text{CIII}] \approx 0.2$  vs  $0.12$ ;  $\text{NV}/H\beta \approx 1.32$  vs  $1.05$ , if total fluxes are considered.

We computed the normalized  $\chi^2_{\nu}$  in the following form, to constrain the value of the metallicity from the values of the diagnostic ratios. For each spectrum  $k$ , and for each component  $c$ , we can write (following Ref. [33]):

$$\chi^2_{\nu, kc}(n_{\text{H}}, U, Z) = \frac{1}{n_{\text{f}}} \sum_{\text{i}} \left( \frac{R_{\text{kci}} - R_{\text{kci, mod}}(n_{\text{H}}, U, Z)}{\delta R_{\text{kci}}} \right)^2 \quad (1)$$

where the summation is made over the available diagnostic ratios. The number of degrees of freedom  $n_{\text{f}}$  is 8 for the composites and 7 for the case of PKS 0226-038 presented in § 4.2. The  $\chi^2_{\nu}$  is computed to the results of the *Cloudy* simulations as a function of  $U$ ,  $n_{\text{H}}$ , and  $Z$  (subscript ‘mod’). The following independent intensity ratios were considered in the summation:  $\text{NV}/\text{CIV}$ ,  $\text{CIV}/\text{HeII} \lambda 1640$ ,  $\text{CIV}/H\beta$ ,  $\text{SiIV}+\text{OIV}] \lambda 1402/\text{CIV}$ ,  $\text{AlIII}/\text{CIV}$ ,  $\text{AlIII}/\text{SiIII}]$ ,  $\text{AlIII}/\text{CIII}]$ ,  $\text{HeII}/H\beta$ ,  $\text{FeII} \lambda 4570/H\beta$ . The ratios were computed for BC, VBC, and total line intensity. Non-detections were treated as upper limits.

<sup>1</sup>  $N(n_{\text{H}}) \times N(U) = 425$ . The overall number of models includes 14 values of metallicity, and for RL and RQ SEDs, is 6,358.

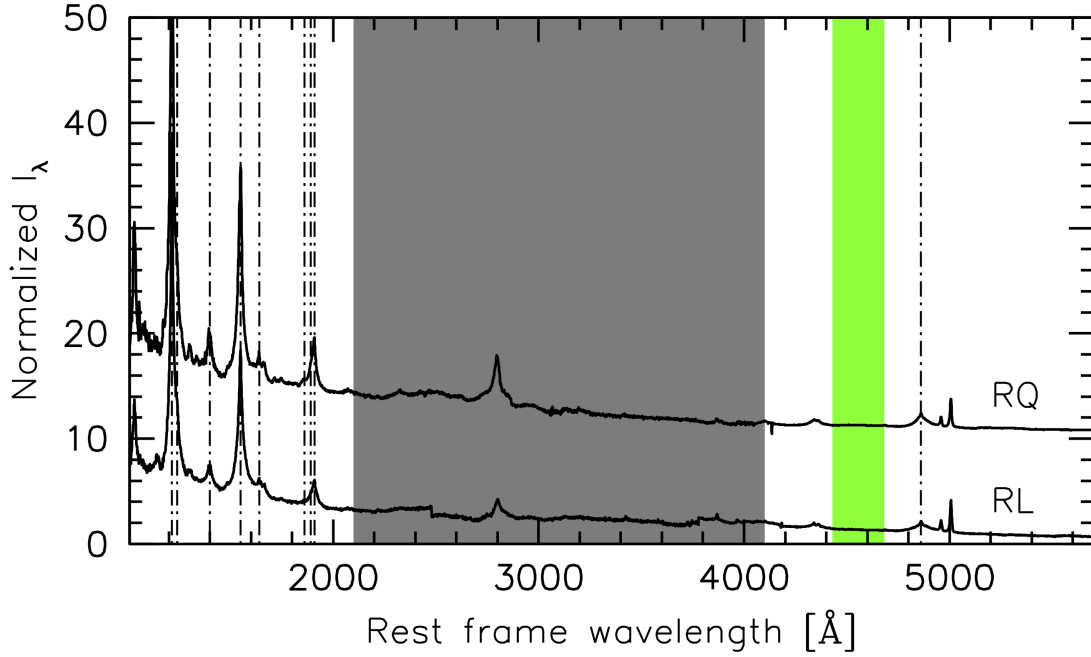


**Figure 2.** The RQ and RL composite spectra covering the optical and the UV domain. The green shaded area marks the range used to measure the FeII $\lambda$ 4570 blend. The grey-shaded region has not been considered in the analysis due to the limited number of available spectra in this region. The RL spectrum has been vertically shifted for clarity. The dot-dashed lines identify the main emission feature included in the non-linear  $\chi^2$  fitting procedures.

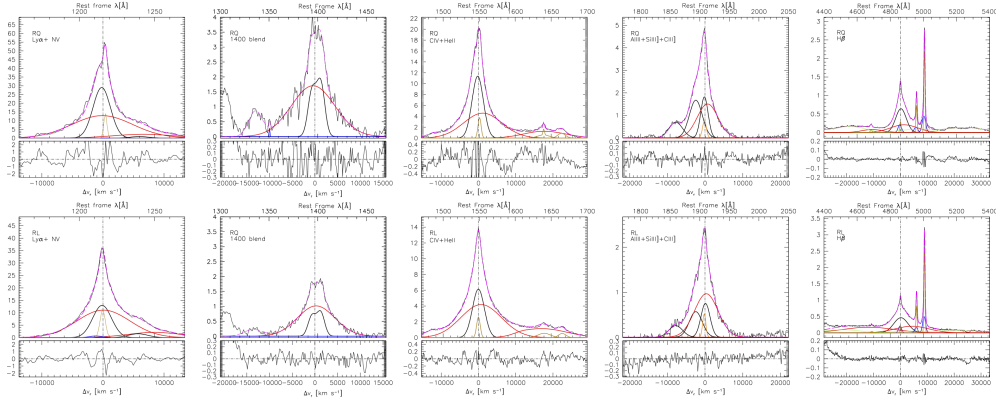


**Figure 3.** Analysis of prominent blends helpful for metallicity diagnostics. Continuum subtracted spectra are shown in the rest frame, with the blend ordered with an increasing wavelength from left to right: the Ly $\alpha$  + Nv blend, SiIV + OIV] $\lambda$ 1402; CIV + HeII; the 1900Å blend made up mainly of AlIII, SiIII, CIII; the H $\beta$  + [OIII] $\lambda\lambda$ 4959,5007 region. Dashed magenta line: model spectrum; thick solid line: broad components; red thick line: very broad components; thin orange lines: narrow components of H $\beta$  and [OIII] $\lambda$ 5007; blue lines: blue-shifted components. Green lines trace the scaled and broadened FeII emission template. The lower panels show the observed minus model residuals in the radial velocity scale.

**Table 1.** Normalised emission line intensities

Line Id.	Comp.	$I/I_{H\beta}$	$I/I_{H\beta}$
		RQ	RL
Nv	BC	$0.257 \pm 0.081$	$0.450 \pm 0.142$
	VBC	$2.604 \pm 0.701$	$1.646 \pm 0.792$
	Total	$1.323 \pm 0.402$	$1.053 \pm 0.320$
[SiIV+OIV] $\lambda$ 1402	BC	$0.667 \pm 0.149$	$0.294 \pm 0.053$
	VBC	$2.237 \pm 0.403$	$0.961 \pm 0.173$
	Total	$1.380 \pm 0.218$	$0.630 \pm 0.100$
CIV	BC	$4.382 \pm 0.620$	$2.545 \pm 0.360$
	VBC	$7.158 \pm 1.012$	$5.840 \pm 0.826$
	Total	$5.643 \pm 0.399$	$4.207 \pm 0.297$
HeII $\lambda$ 1640	BC	$0.228 \pm 0.072$	$0.238 \pm 0.075$
	VBC	$2.099 \pm 0.469$	$1.817 \pm 0.406$
	Total	$1.078 \pm 0.222$	$1.034 \pm 0.213$
AlIII	BC	$0.388 \pm 0.123$	$0.150 \pm 0.046$
	Total	$0.485 \pm 0.100$	$0.156 \pm 0.063$
CIII]	BC	$0.556 \pm 0.124$	$0.291 \pm 0.064$
	VBC	$1.548 \pm 0.346$	$0.951 \pm 0.213$
	Total	$1.007 \pm 0.113$	$0.624 \pm 0.070$
FeII $\lambda$ 4570	Total	$0.344 \pm 0.088$	$0.175 \pm 0.088$
HeII	BC	$\lesssim 0.1$	$\lesssim 0.1$
	VBC	$0.299 \pm 0.152$	$\lesssim 1.299$
	Total	$0.136 \pm 0.068$	$\lesssim 0.655$

Fig. 4 shows the projections of the 3D space  $U$ ,  $n_H$ ,  $Z$ . Each contour in the plane braces elements of the grid of *Cloudy* parameter space that is consistent with the minimum  $\chi^2_{\nu}$  within the uncertainties at  $1\sigma$ ,  $2\sigma$ , and  $3\sigma$  confidence levels.

The distribution of the data points is constrained in a range of  $U$ ,  $n_H$ ,  $Z$ , at very low density, relatively high ionization, and low metallicity. Within the limit in  $U$ , and  $n_H$ , the distribution of  $Z$  is slightly subsolar for the RQ ( $Z \approx 0.5Z_{\odot}$ ), and even more subsolar for the radio loud, ( $Z \approx 0.1Z_{\odot}$ ). There is a relatively broad range of density and ionization parameters and metallicities that are consistent within  $2\sigma$  confidence level from the minimum  $\chi^2$ . This is probably a reflection of the stratified nature of the emitting region in Population B and the intrinsic heterogeneity of the composites.

The values reported in Table 2 for the sub-regions confirm the validity of the virial scenario, with  $U$  increasing by a factor  $\gtrsim 10$  between BLR and VBLR. The derived density is not changing strongly, as implied by the strong CIII] VBC. Since the distance from the center of gravity scales with the inverse of the velocity dispersion squared (i.e.,  $r \propto \text{FWHM}^{-2}$ , we might expect that  $U/U_{\text{BLR}} \sim \text{FWHM}_{\text{VBLR}}^4/\text{FWHM}_{\text{BLR}}^4 \sim (2.32 - 2.55)^4 \sim 29 - 42$ . The  $U$  values reported in Table 2 indicate ratios between 1 – 2 orders of magnitudes, consistent with the ones expected from a virial velocity field.

The  $Z$  values all fall in ranges that are consistent. The results for the sub-regions should be seen with some care, as the VBC measurements are difficult for HeII, HeII $\lambda$ 1640, NV. The fairly high metallicity value for RQ VBLR is due to several line ratios being consistently higher than for the RL case: CIV/ $H\beta$ , (SiIV+OIV] $\lambda$ 1402)/CIV, (SiIV+OIV] $\lambda$ 1402)/HeII $\lambda$ 1640, and NV/HeII $\lambda$ 1640 are between 30% and a factor 2 higher for the VBLR of RQ than of RL. This epitomizes the need for very accurate measurements on the line profiles.

These results can be compared with the ones derived from the analysis of the Sloan composite spectrum [46]. Values of the intensity ratios reported in their Table 2, and the assumption of typical 10% uncertainties for most ratios, do not provide any constraint on  $Z$ , and loose constraints on density ( $\log n_H \sim 9.5^{+1.5}_{-2.5}$ ) and ionization ( $\log U \sim -1.75 - -0.5$ ). Averaging the full dataset of a large color-based spectroscopic survey presents major hindrances. Spectral bins are likely to be associated with intrinsic differences in  $Z$ . Building a composite combines all survey spectra with a

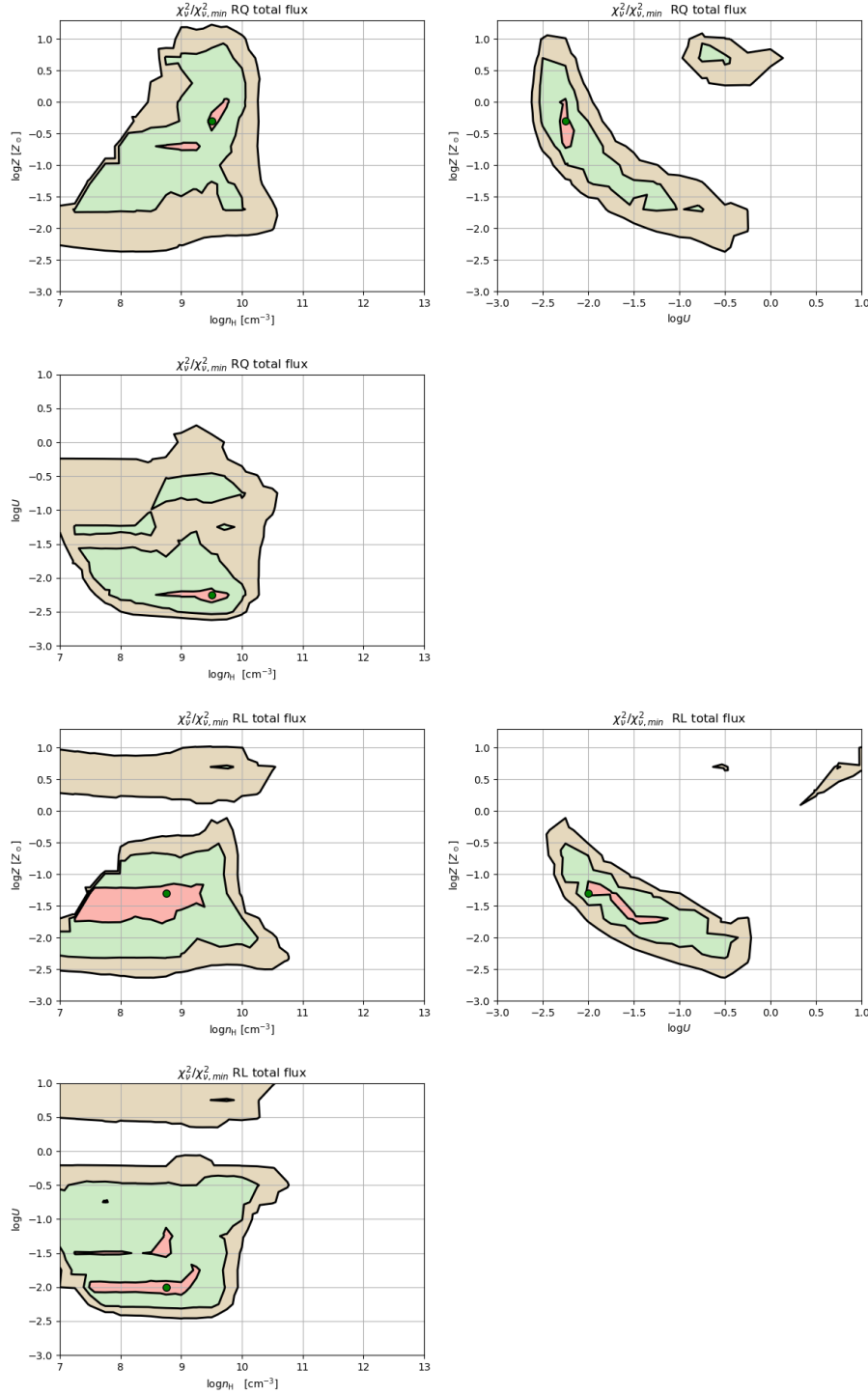


**Figure 4.** Projections of the 3D parameter space  $n_{\text{H}}, U, Z$ . Isophotal contour traces the 1,2,3 $\sigma$  confidence levels; the green spot identifies the values of  $n_{\text{H}}, U, Z$  yielding the minimum  $\chi^2_{\text{V}}$ . The upper panels are for RQ, lower panels are for RL. Regions of the parameter space where  $[\text{O III}]\lambda 5007 / \text{H}\beta > 0.1$  have been assigned a very high  $\chi^2_{\text{V}}$ .

weight proportional to the relative prevalence of each spectral type [e.g., 13]. Since the most populated spectral bins along the sequence is B1, with A2 the second most populated [15,47], the appearance of the composite spectrum is resembling the Pop. B RQ composite is some key features, and A2 in

**Table 2.** Derived values of  $U$ ,  $Z$ ,  $n_{\text{H}}$  and  $1\sigma$  ranges<sup>a</sup>

Class	Region	$\log U$	$\Delta \log U$	$\log Z$	$\Delta \log Z$	$\log n_{\text{H}}$	$\Delta \log n_{\text{H}}$
RQ	Tot.	-2.25	-2.25 – -2.25	-0.30	-0.70 – 0.00	9.50	8.50 – 9.75
RQ	BLR	-2.25	-2.25 – -1.75	0.30	-0.70 – 1.00	10.25	9.25 – 10.75
RQ	VBLR	0.00	0.00 – 0.00	0.70	0.70 – 0.70	9.50	9.50 – 9.75
RL	Tot.	-2.00	-2.00 – -0.75	-1.30	-2.00 – -1.30	8.75	7.00 – 9.75
RL	BLR	-1.50	-2.00 – -0.75	-1.70	-2.00 – -1.00	10.25	8.75 – 10.50
RL	VBLR	-0.75	-1.25 – -0.25	-2.00	-2.00 – -1.70	7.75	7.00 – 10.25

<sup>a</sup>: ionization parameter  $U$ , abundance  $Z$  in solar units, and Hydrogen particle density  $n_{\text{H}}$  in units of  $\text{cm}^{-3}$ . The ranges are defined by the limiting elements of the model grid that are compatible with the minimum  $\chi^2_{\nu}$  within  $1\sigma$  confidence level.

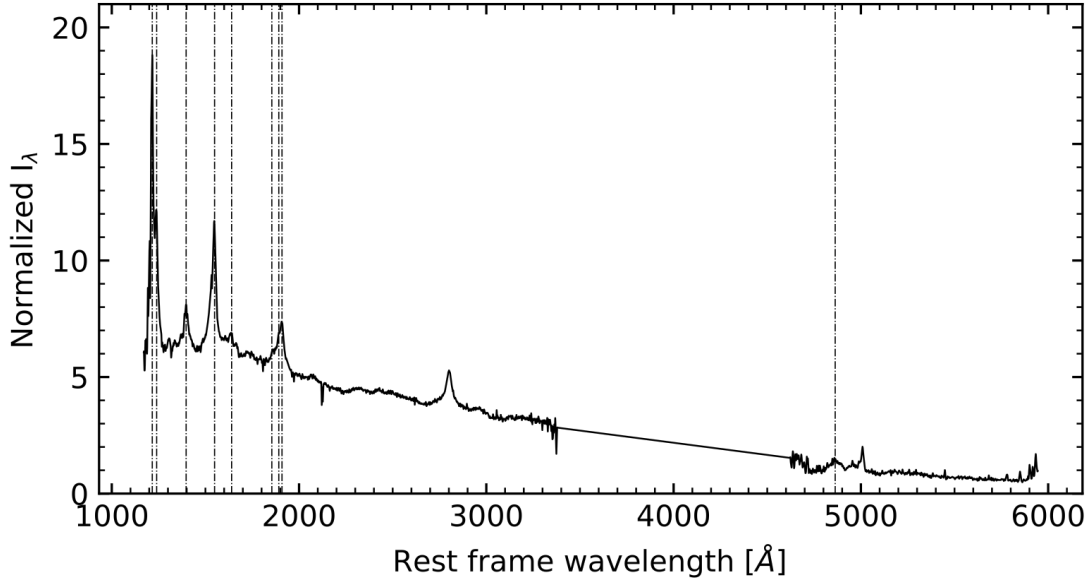


**Figure 5.** The spectrum of PKS 0226-038 in the optical and the UV domain. The dot-dashed lines identify the main emission features included in the non-linear  $\chi^2$  fitting procedures. The straight line traces a range where data are unavailable for this source.

others. For example, the moderate  $\text{FeII}/\text{H}\beta$  and  $\text{SiIV}+\text{OIV}(\lambda 1402)/\text{CIV}$  values are consistent with solar or supersolar  $Z$ . The composite is yielding line ratios that reflect a combination of physical properties from individual spectra; on the other hand, it does not reflect the spectral diversity of a large population of type-1 AGN, as extreme sources are just a minority ( $\lesssim 5\%$ ; Fig. 1).

#### 4.2. A typical RL source at high $z$

PKS 0226-038 is a luminous jetted source at the cosmic noon ( $z \approx 2.06922$ ;  $M_{\text{B}} \approx -28.0$ , and Kellermann's radio loudness parameter [48],  $R_{\text{K}} \sim 10^3$ ). Its optical and UV spectrum is markedly different from the Population B composite at low  $z$ :  $\text{CIII}$  is weaker,  $\text{FeII}$  stronger, and  $\text{AlIII}$  is almost as strong as  $\text{CIV}$  (Fig. 5). No diagnostic based on  $\text{NV}$  and  $\text{HeII}$  is available in this case. The measured diagnostic ratios are reported in Table 3. The uncertainties were assumed to be  $\approx 10\%$  for the intensities normalized to  $\text{H}\beta$  save for  $\text{CIV}/\text{H}\beta$  that is affected by a re-scaling ( $\approx 20\%$ ) and for  $\text{FeII}\lambda 4570$  for which  $\delta R_{\text{FeII}} = 0.1$  was assumed. In this case, the  $\text{FeII}\lambda 4570$  (Fig. 5) is partly missing because of a telluric absorption. The  $\text{FeII}$  optical emission is well-represented by a "solid" template with fixed multiplet ratios.

The derived values of the metallicity are well constrained with minimum  $\chi^2$  obtained for  $\log Z/Z_{\odot} \approx 1$ , with  $1\sigma$  uncertainty equal to 0.3 dex. The ionization parameter  $\log U \approx -2.75$  and density  $\log n_{\text{H}} \sim 11.75 [\text{cm}^{-3}]$  are significantly lower and higher with respect to the values at low- $z$ .



**Table 3.** Diagnostic line ratios measured on the PKS 0226-038 spectrum<sup>a</sup>

Ratio Id.	Value
CIV/HeII $\lambda$ 1640	$4.436 \pm 0.627$
(SiIV+OIV) $\lambda$ 1402)/CIV	$0.361 \pm 0.051$
(SiIV+OIV) $\lambda$ 1402)/HeII $\lambda$ 1640	$1.603 \pm 0.227$
CIV/H $\beta$	$3.460 \pm 0.720$
AlIII/CIV	$0.986 \pm 0.139$
AlIII/SiIII]	$0.642 \pm 0.091$
SiIII]/CIII]	$6.034 \pm 0.853$
$R_{\text{FeII}}$	$0.62 \pm 0.10$

<sup>a</sup>Line ratios refer to the total flux of the full broad line profiles.

The three parameters reflect the moderate  $R_{\text{FeII}}$ , high AlIII/CIV (yielding low ionization and high  $Z$ ), and low CIII]/SiIII] (implying a high density).

## 5. Discussion: metal enrichment along the quasar Main Sequence

Several basic results emerge from the present analysis:

- 1 RQ Pop. B sources show slightly sub-solar or solar metallicities; in the same spectral bin along the MS, RL sources show definitely sub-solar chemical abundances, lower with respect to RQ. The difference is not marginal and is supported by several diagnostic indicators consistently observed to be lower in RL sources. It is also consistent with the location of the RL template in the MS, displaced toward broader H $\beta$  and lower  $R_{\text{FeII}}$  with respect to the RQ one.
- 2 there is an important difference in properties at the extremes of the E1 MS: here, we focused only on the low- $R_{\text{FeII}}$  extreme deriving sub-solar metallicity. However, highly-supersolar  $Z$  estimates were derived at the other end of the MS, with  $R_{\text{FeII}} \gtrsim 1$  [33,34].

The first result is not completely unexpected, since a similar analysis yielded slightly sub-solar abundances for NGC 1275 [49] and Pop. B sources are known to have similar intensity ratios [50].

The origin of the RQ and RL  $Z$  difference is likely associated with a difference in sample/host galaxy evolutionary history. At the modest accretion rates required to sustain the low Eddington ratio of B1 sources, there is no need to invoke "cataclysmic" events such as recent, major wet mergers to explain the AGN luminosity via super-Eddington accretion rates [51], and accretion material could be provided via stellar mass loss in early-type galaxies [52]. The general impression of low- $z$  Population B is that of fairly evolved systems, past their prime of accretion events [53]. This impression, is further reinforced in the case of radio-loud sources, where sub-parsec binary black holes at the stable end of their in-spiral phase are relatively frequent [54].

The gradient in chemical composition is also no surprise. While it is possible to account for an increase in FeII along the sequence only based on ionization degree and density [55], a thorough quantitative assessment requires also a change in chemical composition [9]. We pass from sources where singly ionized iron emission is barely detected to sources where it dominates the thermal balance of the emitting regions, overwhelming the entire Balmer line emission.

The case of the high- $z$  RL source PKS 0226-038 signifies the co-existence of powerful relativistic ejections and BLR physical conditions typical of sources radiating at  $L/L_{\text{Edd}} \gtrsim 0.1 - 0.2$  (Population A according to Ref. [14]). It is known for a long time that the radio-loud fraction among AGN increases with redshift [56,57]. However, the realization of the high prevalence of unambiguously jetted AGN at  $z \gtrsim 1$  radiating at high  $L/L_{\text{Edd}}$  is a recent result. The Eddington ratio of PKS 0226-038 is  $\log L/L_{\text{Edd}} \approx -0.43$ . It belongs to the spectral type B2, that include sources in the  $R_{\text{FeII}}$  range 0.5 - 1, and with moderate accretion rate. Strong FeII emission is a rather rare occurrence among RLs at low- $z$  (especially in Fanaroff-Riley II sources, [17]), it is frequently found at high redshift (Ref. [58],

and article in preparation), along with higher  $L/L_{\text{Edd}}$ . This is probably a consequence of the increase in average accretion rate at the epochs corresponding to the cosmic noon [59–61], and much beyond. Indeed, highly accreting jetted sources are being discovered up to redshift  $\approx 6$  [62,63].

## 6. Conclusions

This pilot work revealed a population of quasars with slightly sub-solar abundances. We can infer a metallicity trend along the quasar MS on the basis of previous results and of the analysis presented in this paper, supporting the assumptions in the study of Panda et al. [9], although the MS-oriented analysis has been yet focused only on the spectral types, B1 and extreme Population A. Full analysis for individual spectral types isolated along the MS [16] is still needed. Special attention should also be devoted to high- $z$  high- $L$  sources. At high- $z$ , sample selection effects could be even more important, excluding a population of sources on the basis of their low accretion rate [64]. At high luminosities, wind effects are expected to be maximized and may introduce another factor in the chemical enrichment of the broad-line emitting gas.

**Author Contributions:** All authors contributed equally to this paper.

**Acknowledgments:** SP acknowledges the financial support from the Conselho Nacional de Desenvolvimento Científico e Tecnológico (CNPq) Fellowship (164753/2020-6) and the computational facility at Nicolaus Copernicus Astronomical Center in Warsaw, Poland where the *Cloudy* simulations presented in this work were performed.

**Conflicts of Interest:** The authors declare no conflict of interest.

## Abbreviations

The following abbreviations are used in this manuscript:

AGN	Active Galactic Nucleus
BC	Broad Component
BLR	Broad Line Region
FWHM	Full Width Half-Maximum
MS	Main Sequence
NLSy1	Narrow-Line Seyfert 1
RL	Radio loud
RQ	Radio quiet
SDSS	Sloan Digital Sky Survey
SED	Spectral energy distribution
S/N	Signal-to-noise ratio
VBC	Very Broad Component
VBLR	Very Broad Line Region

1. Netzer, H. AGN emission lines. *Active Galactic Nuclei*; R. D. Blandford, H. Netzer, L. Woltjer, T. J.-L. Courvoisier, & M. Mayor., Ed., 1990, pp. 57–160.
2. Peterson, B.M. *An Introduction to Active Galactic Nuclei*; Cambridge University Press, 1997.
3. Osterbrock, D.E.; Ferland, G.J. *Astrophysics of gaseous nebulae and active galactic nuclei*; University Science Books: Mill Valley, CA, 2006.
4. Kaler, J.B. *Stars and their Spectra, An Introduction to the Spectral Sequence*; Cambridge University Press, 1997.
5. Peterson, B.M. Measuring the Masses of Supermassive Black Holes. *SpScieRev* **2014**, *183*, 253–275. doi:10.1007/s11214-013-9987-4.
6. Du, P.; Wang, J.M.; Hu, C.; Ho, L.C.; Li, Y.R.; Bai, J.M. The Fundamental Plane of the Broad-line Region in Active Galactic Nuclei. *ApJL* **2016**, *818*, L14, [1601.01391]. doi:10.3847/2041-8205/818/1/L14.
7. Marziani, P.; Sulentic, J.W.; Stirpe, G.M.; Dultzin, D.; Del Olmo, A.; Martínez-Carballo, M.A. Blue outliers among intermediate redshift quasars. *ApSS* **2016**, *361*, 3, [1511.07138]. doi:10.1007/s10509-015-2590-2.
8. Panda, S.; Czerny, B.; Adhikari, T.P.; Hryniewicz, K.; Wildy, C.; Kuraszekiewicz, J.; Śniegowska, M. Modeling of the Quasar Main Sequence in the Optical Plane. *The Astrophysical Journal* **2018**, *866*, 115. doi:10.3847/1538-4357/aae209.
9. Panda, S.; Marziani, P.; Czerny, B. The Quasar Main Sequence Explained by the Combination of Eddington Ratio, Metallicity, and Orientation. *ApJ* **2019**, *882*, 79, [arXiv:astro-ph.HE/1905.01729]. doi:10.3847/1538-4357/ab3292.
10. Ferland, G.J.; Done, C.; Jin, C.; Landt, H.; Ward, M.J. State-of-the-art AGN SEDs for photoionization models: BLR predictions confront the observations. *MNRAS* **2020**, *494*, 5917–5922, [arXiv:astro-ph.HE/2004.11873]. doi:10.1093/mnras/staa1207.
11. Panda, S. Physical Conditions in the Broad-line Regions of Active Galaxies. PhD thesis, Polish Academy of Sciences, Institute of Physics, 2021.
12. Boroson, T.A.; Green, R.F. The Emission-Line Properties of Low-Redshift Quasi-stellar Objects. *ApJS* **1992**, *80*, 109. doi:10.1086/191661.
13. Sulentic, J.; Marziani, P. Quasars in the 4D Eigenvector 1 Context: a stroll down memory lane. *Frontiers in Astronomy and Space Sciences* **2015**, *2*, 6, [1506.01276]. doi:10.3389/fspas.2015.00006.
14. Sulentic, J.W.; Marziani, P.; Dultzin-Hacyan, D. Phenomenology of Broad Emission Lines in Active Galactic Nuclei. *ARA&A* **2000**, *38*, 521–571. doi:10.1146/annurev.astro.38.1.521.
15. Shen, Y.; Ho, L.C. The diversity of quasars unified by accretion and orientation. *Nat* **2014**, *513*, 210–213, [1409.2887]. doi:10.1038/nature13712.
16. Sulentic, J.W.; Marziani, P.; Zamanov, R.; Bachev, R.; Calvani, M.; Dultzin-Hacyan, D. Average Quasar Spectra in the Context of Eigenvector 1. *ApJL* **2002**, *566*, L71–L75, [arXiv:astro-ph/0201362]. doi:10.1086/339594.
17. Zamfir, S.; Sulentic, J.W.; Marziani, P. New insights on the QSO radio-loud/radio-quiet dichotomy: SDSS spectra in the context of the 4D eigenvector1 parameter space. *MNRAS* **2008**, *387*, 856–870, [0804.0788]. doi:10.1111/j.1365-2966.2008.13290.x.
18. Marziani, P.; Berton, M.; Panda, S.; Bon, E. Optical Singly-Ionized Iron Emission in Radio-Quiet and Relativistically Jetted Active Galactic Nuclei. *Universe* **2021**, *7*, 484, [arXiv:astro-ph.GA/2112.02632]. doi:10.3390/universe7120484.
19. Marziani, P.; Sulentic, J.W.; Zamanov, R.; Calvani, M.; Dultzin-Hacyan, D.; Bachev, R.; Zwitter, T. An Optical Spectroscopic Atlas of Low-Redshift Active Galactic Nuclei. *ApJS* **2003**, *145*, 199–211. doi:10.1086/346025.
20. Sulentic, J.W.; Bachev, R.; Marziani, P.; Negrete, C.A.; Dultzin, D. C IV  $\lambda$ 1549 as an Eigenvector 1 Parameter for Active Galactic Nuclei. *ApJ* **2007**, *666*, 757–777, [arXiv:astro-ph/0705.1895]. doi:10.1086/519916.
21. Marziani, P.; Sulentic, J.W.; Stirpe, G.M.; Zamfir, S.; Calvani, M. VLT/ISAAC spectra of the H $\beta$  region in intermediate-redshift quasars. III. H $\beta$  broad-line profile analysis and inferences about BLR structure. *A&Ap* **2009**, *495*, 83–112, [0812.0251]. doi:10.1051/0004-6361:200810764.
22. Snedden, S.A.; Gaskell, C.M. The Case for Optically Thick High-Velocity Broad-Line Region Gas in Active Galactic Nuclei. *ApJ* **2007**, *669*, 126–134. doi:10.1086/521290.
23. Peterson, B.M.; Ferland, G.J. An accretion event in the Seyfert galaxy NGC 5548. *Nature* **1986**, *324*, 345–347. doi:10.1038/324345a0.

24. Brotherton, M.S.; Wills, B.J.; Francis, P.J.; Steidel, C.C. The intermediate line region of QSOs. *ApJ* **1994**, *430*, 495–504. doi:10.1086/174425.
25. Sulentic, J.W.; Zwitter, T.; Marziani, P.; Dultzin-Hacyan, D. Eigenvector 1: An Optimal Correlation Space for Active Galactic Nuclei. *ApJL* **2000**, *536*, L5–L9, [arXiv:astro-ph/0005177]. doi:10.1086/312717.
26. Wang, J.; Li, Y. Strong Response of the Very Broad H $\beta$  Emission Line in the Luminous Radio-quiet Quasar PG 1416-129. *ApJL* **2011**, *742*, L12, [1110.4701]. doi:10.1088/2041-8205/742/1/L12.
27. Zamfir, S.; Sulentic, J.W.; Marziani, P.; Dultzin, D. Detailed characterization of H $\beta$  emission line profile in low-*z* SDSS quasars. *MNRAS* **2010**, *403*, 1759, [0912.4306]. doi:10.1111/j.1365-2966.2009.16236.x.
28. Kriss, G. Fitting Models to UV and Optical Spectral Data. *Astronomical Data Analysis Software and Systems III, A.S.P. Conference Series* **1994**, *61*, 437.
29. Negrete, A.; Dultzin, D.; Marziani, P.; Sulentic, J. BLR Physical Conditions in Extreme Population A Quasars: a Method to Estimate Central Black Hole Mass at High Redshift. *ApJ* **2012**, *757*, 62, [arXiv:astro-ph.CO/1107.3188].
30. Negrete, C.A.; Dultzin, D.; Marziani, P.; Sulentic, J.W. Reverberation and Photoionization Estimates of the Broad-line Region Radius in Low-*z* Quasars. *ApJ* **2013**, *771*, 31, [arXiv:astro-ph.CO/1305.4574]. doi:10.1088/0004-637X/771/1/31.
31. Marziani, P.; Sulentic, J.W.; Negrete, C.A.; Dultzin, D.; Del Olmo, A.; Martínez Carballo, M.A.; Zwitter, T.; Bachev, R. UV spectral diagnostics for low redshift quasars: estimating physical conditions and radius of the broad line region. *ApSS* **2015**, *356*, 339–346, [1410.3146]. doi:10.1007/s10509-014-2136-z.
32. Chieffi, A.; Limongi, M. Pre-supernova Evolution of Rotating Solar Metallicity Stars in the Mass Range 13-120 M $_{\odot}$  and their Explosive Yields. *ApJ* **2013**, *764*, 21. doi:10.1088/0004-637X/764/1/21.
33. Śniegowska, M.; Marziani, P.; Czerny, B.; Panda, S.; Martínez-Aldama, M.L.; del Olmo, A.; D’Onofrio, M. High Metal Content of Highly Accreting Quasars. *ApJ* **2021**, *910*, 115, [arXiv:astro-ph.HE/2009.14177]. doi:10.3847/1538-4357/abe1c8.
34. Garnica, K.; Negrete, C.A.; Marziani, P.; Dultzin, D.; Śniegowska, M.; Panda, S. High metal content of highly accreting quasars: Analysis of an extended sample. *A&A* **2022**, *667*, A105, [arXiv:astro-ph.GA/2208.02387]. doi:10.1051/0004-6361/202142837.
35. Ferland, G.J.; Chatzikos, M.; Guzmán, F.; Lykins, M.L.; van Hoof, P.A.M.; Williams, R.J.R.; Abel, N.P.; Badnell, N.R.; Keenan, F.P.; Porter, R.L.; Stancil, P.C. The 2017 Release Cloudy. *RevMexA&Ap* **2017**, *53*, 385–438, [arXiv:astro-ph.GA/1705.10877].
36. Laor, A.; Fiore, F.; Elvis, M.; Wilkes, B.J.; McDowell, J.C. The Soft X-Ray Properties of a Complete Sample of Optically Selected Quasars. II. Final Results. *ApJ* **1997**, *477*, 93–+, [arXiv:astro-ph/9609164]. doi:10.1086/303696.
37. Baldwin, J.; Ferland, G.; Korista, K.; Verner, D. Locally Optimally Emitting Clouds and the Origin of Quasar Emission Lines. *ApJL* **1995**, *455*, L119+, [arXiv:astro-ph/9510080]. doi:10.1086/309827.
38. Korista, K.; Baldwin, J.; Ferland, G.; Verner, D. An Atlas of Computed Equivalent Widths of Quasar Broad Emission Lines. *ApJS* **1997**, *108*, 401–+, [arXiv:astro-ph/9611220]. doi:10.1086/312966.
39. Guo, H.; Shen, Y.; He, Z.; Wang, T.; Liu, X.; Wang, S.; Sun, M.; Yang, Q.; Kong, M.; Sheng, Z. Understanding Broad Mg II Variability in Quasars with Photoionization: Implications for Reverberation Mapping and Changing-look Quasars. *ApJ* **2020**, *888*, 58, [arXiv:astro-ph.GA/1907.06669]. doi:10.3847/1538-4357/ab5db0.
40. Marziani, P.; Sulentic, J.W. Evidence for a very broad line region in PG 1138+222. *ApJ* **1993**, *409*, 612–616, [arXiv:astro-ph/9210005]. doi:10.1086/172692.
41. Marziani, P.; Olmo, A.d.; Negrete, C.A.; Dultzin, D.; Piconcelli, E.; Vietri, G.; Martínez-Aldama, M.L.; D’Onofrio, M.; Bon, E.; Bon, N.; Deconto Machado, A.; Stirpe, G.M.; Buendia Rios, T.M. The Intermediate-ionization Lines as Virial Broadening Estimators for Population A Quasars. *ApJS* **2022**, *261*, 30, [arXiv:astro-ph.GA/2205.07034]. doi:10.3847/1538-4365/ac6fd6.
42. Sulentic, J.W.; del Olmo, A.; Marziani, P.; Martínez-Carballo, M.A.; D’Onofrio, M.; Dultzin, D.; Perea, J.; Martínez-Aldama, M.L.; Negrete, C.A.; Stirpe, G.M.; Zamfir, S. What does CIV $\lambda$ 1549 tell us about the physical driver of the Eigenvector quasar sequence? *A&A* **2017**, *608*, A122, [1708.03187]. doi:10.1051/0004-6361/201630309.
43. Marziani, P.; Zamanov, R.K.; Sulentic, J.W.; Calvani, M. Searching for the physical drivers of eigenvector 1: influence of black hole mass and Eddington ratio. *MNRAS* **2003**, *345*, 1133–1144, [arXiv:astro-ph/0307367]. doi:10.1046/j.1365-2966.2003.07033.x.

44. Punsly, B. The Redshifted Excess in Quasar C IV Broad Emission Lines. *ApJ* **2010**, *713*, 232–238, [[1002.4681](#)]. doi:10.1088/0004-637X/713/1/232.
45. Marziani, P.; Berton, M.; Panda, S.; Bon, E. Optical Singly-Ionized Iron Emission in Radio-Quiet and Relativistically Jetted Active Galactic Nuclei. *Universe* **2021**, *7*, 484, [[arXiv:astro-ph.GA/2112.02632](#)]. doi:10.3390/universe7120484.
46. Vanden Berk, D.E.; Wilhite, B.C.; Kron, R.G.; Anderson, S.F.; Brunner, R.J.; Hall, P.B.; Ivezić, Ž.; Richards, G.T.; Schneider, D.P.; York, D.G.; Brinkmann, J.V.; Lamb, D.Q.; Nichol, R.C.; Schlegel, D.J. The Ensemble Photometric Variability of ~25,000 Quasars in the Sloan Digital Sky Survey. *ApJ* **2004**, *601*, 692–714, [[astro-ph/0310336](#)]. doi:10.1086/380563.
47. Marziani, P.; Sulentic, J.W.; Plauchu-Frayn, I.; del Olmo, A. Is Mg II 2800 a Reliable Virial Broadening Estimator for Quasars? *AAp* **2013**, *555*, 89, 16pp, [[arXiv:astro-ph.CO/1305.1096](#)].
48. Kellermann, K.I.; Sramek, R.; Schmidt, M.; Shaffer, D.B.; Green, R. VLA Observations of Objects in the Palomar Bright Quasar Survey. *AJ* **1989**, *98*, 1195. doi:10.1086/115207.
49. Punsly, B.; Marziani, P.; Bennert, V.N.; Nagai, H.; Gurwell, M.A. Revealing the Broad Line Region of NGC 1275: The Relationship to Jet Power. *ApJ* **2018**, *869*, 143, [[1810.11716](#)]. doi:10.3847/1538-4357/aaec75.
50. Marziani, P.; Sulentic, J.W.; Negrete, C.A.; Dultzin, D.; Zamfir, S.; Bachev, R. Broad-line region physical conditions along the quasar eigenvector 1 sequence. *MNRAS* **2010**, *409*, 1033–1048, [[arXiv:astro-ph.CO/1007.3187](#)]. doi:10.1111/j.1365-2966.2010.17357.x.
51. D’Onofrio, M.; Marziani, P. A multimessenger view of galaxies and quasars from now to mid-century. *Frontiers in Astronomy and Space Sciences* **2018**, *5*, 31, [[arXiv:astro-ph.GA/1807.07435](#)]. doi:10.3389/fspas.2018.00031.
52. Padovani, P.; Matteucci, F. Stellar Mass Loss in Elliptical Galaxies and the Fueling of Active Galactic Nuclei. *ApJ* **1993**, *416*, 26. doi:10.1086/173212.
53. Fraix-Burnet, D.; Marziani, P.; D’Onofrio, M.; Dultzin, D. The Phylogeny of Quasars and the Ontogeny of Their Central Black Holes. *Frontiers in Astronomy and Space Sciences* **2017**, *4*, 1. doi:10.3389/fspas.2017.00001.
54. Krause, M.G.H.; Shabala, S.S.; Hardcastle, M.J.; Bicknell, G.V.; Böhringer, H.; Chon, G.; Nawaz, M.A.; Sarzi, M.; Wagner, A.Y. How frequent are close supermassive binary black holes in powerful jet sources? *MNRAS* **2019**, *482*, 240–261, [[arXiv:astro-ph.HE/1809.04050](#)]. doi:10.1093/mnras/sty2558.
55. Marziani, P.; Sulentic, J.W.; Zwitter, T.; Dultzin-Hacyan, D.; Calvani, M. Searching for the Physical Drivers of the Eigenvector 1 Correlation Space. *ApJ* **2001**, *558*, 553–560, [[arXiv:astro-ph/0105343](#)]. doi:10.1086/322286.
56. Padovani, P.; Ghisellini, G.; Fabian, A.C.; Celotti, A. Radio-loud AGN and the extragalactic gamma-ray background. *MNRAS* **1993**, *260*, L21–L24. doi:10.1093/mnras/260.1.L21.
57. La Franca, F.; Gregorini, L.; Cristiani, S.; de Ruiter, H.; Owen, F. Deep VLA Observations of an Optically Selected Sample of Intermediate Redshift QSOs and the Optical Luminosity Function of the Radio Loud QSOs. *AJ* **1994**, *108*, 1548. doi:10.1086/117176.
58. Deconto-Machado, A.; del Olmo, A.; Marziani, P.; Perea, J.; Stirpe, G.M. High-redshift quasars along the Main Sequence. *arXiv e-prints* **2022**, p. arXiv:2211.03853, [[arXiv:astro-ph.GA/2211.03853](#)].
59. Cavaliere, A.; Vittorini, V. The Fall of the Quasar Population. *ApJ* **2000**, *543*, 599–610, [[arXiv:astro-ph/0006194](#)]. doi:10.1086/317155.
60. Marconi, A.; Risaliti, G.; Gilli, R.; Hunt, L.K.; Maiolino, R.; Salvati, M. Local supermassive black holes, relics of active galactic nuclei and the X-ray background. *MNRAS* **2004**, *351*, 169–185, [[arXiv:astro-ph/astro-ph/0311619](#)]. doi:10.1111/j.1365-2966.2004.07765.x.
61. Hopkins, P.F.; Hernquist, L.; Cox, T.J.; Di Matteo, T.; Robertson, B.; Springel, V. A Unified, Merger-driven Model of the Origin of Starbursts, Quasars, the Cosmic X-Ray Background, Supermassive Black Holes, and Galaxy Spheroids. *ApJS* **2006**, *163*, 1–49, [[astro-ph/0506398](#)]. doi:10.1086/499298.
62. Bañados, E.; Mazzucchelli, C.; Momjian, E.; Eilers, A.C.; Wang, F.; Schindler, J.T.; Connor, T.; Andika, I.T.; Barth, A.J.; Carilli, C.; Davies, F.B.; Decarli, R.; Fan, X.; Farina, E.P.; Hennawi, J.F.; Pensabene, A.; Stern, D.; Venemans, B.P.; Wenzl, L.; Yang, J. The Discovery of a Highly Accreting, Radio-loud Quasar at  $z = 6.82$ . *ApJ* **2021**, *909*, 80, [[arXiv:astro-ph.CO/2103.03295](#)]. doi:10.3847/1538-4357/abe239.
63. Ighina, L.; Caccianiga, A.; Moretti, A.; Belladitta, S.; Broderick, J.W.; Drouart, G.; Leung, J.K.; Seymour, N. New radio-loud QSOs at the end of the Re-ionization epoch. *MNRAS* **2023**, *519*, 2060–2068, [[arXiv:astro-ph.GA/2212.06168](#)]. doi:10.1093/mnras/stac3668.

64. Sulentic, J.W.; Marziani, P.; del Olmo, A.; Dultzin, D.; Perea, J.; Alenka Negrete, C. GTC spectra of  $z \approx 2.3$  quasars: comparison with local luminosity analogs. *A&A* **2014**, *570*, A96, [1406.5920]. doi:10.1051/0004-6361/201423975.

© 2023 by the authors. Submitted to *Galaxies* for possible open access publication under the terms and conditions of the Creative Commons Attribution (CC BY) license (<http://creativecommons.org/licenses/by/4.0/>).